



OPEN Triaxial behavior and microstructural insights of loose sandy soil stabilized with alkali activated slag

Mohammad Banaian, Seyed Mohammad Fattahi✉, Abbas Soroush & Alireza Komaei

This study investigates the mechanical and microstructural properties of loose sandy soil stabilized with alkali-activated Ground Granulated Blast Furnace Slag (GGBFS). To examine the effects of varying GGBFS contents, curing times, and confining pressures on mechanical behavior, undrained triaxial and unconfined compressive strength (UCS) tests were conducted. Microstructural analyses using FE-SEM, EDX, and FTIR were performed to elucidate the nature and development of cementation. The results of mechanical behavior demonstrate that even with limited GGBFS content (1–6%), the treated samples exhibited significant improvements in strength, stiffness, and energy absorption, underscoring the efficiency of alkali-activated GGBFS as a soil stabilizer. Moreover, mechanical parameters from triaxial tests revealed a nearly constant internal friction angle with increasing GGBFS content and curing duration, while cohesion showed remarkable enhancement. A strong linear correlation between UCS and cohesion was also identified, enabling cost-effective estimation of shear strength parameters. These findings highlight the potential of alkali-activated GGBFS for improving granular soils, offering practical implications for sustainable geotechnical applications, particularly in road construction.

Keywords Soil improvement, Alkali-activated slag (GGBFS), Mechanical behavior, Mechanical strength parameters, Microstructural analysis

The successful construction and maintenance of road infrastructure rely significantly on the quality and stability of the underlying soil layers, particularly the subgrade, which serves as the foundation for the road surface. Loose sands and silts, encountered in some road construction projects as subgrade material, are characterized by their non-cohesive nature, leading to poor load-bearing capacity and susceptibility to excessive settlement¹. Consequently, it becomes imperative to address the engineering properties of loose sands and silts through effective soil improvement techniques to attain the desired performance and durability of road infrastructure in such environments².

One effective method for soil improvement involves chemical treatment, where conventional stabilizers like ordinary Portland cement (OPC) or lime are mixed with soil. This process promotes inter-particle cementation, thereby enhancing the mechanical characteristics of the soil and mitigating its compressibility³.

OPC has experienced notable annual production growth. In 2015, global OPC production reached 4.6 billion tons⁴, and predictions indicate an ascent to approximately 4.83 billion tons by 2030^{4,5}. However, this excessive reliance on OPC has given rise to significant environmental concerns. The production of 1 ton of OPC produces about 1 ton of CO₂, contributing to approximately 5% to 8% of global anthropogenic CO₂ emissions. Moreover, this production process involves an energy consumption of 5000 MJ^{6,7}. Furthermore, OPC production depletes natural resources as it consumes significant amounts of raw materials like limestone and clay⁸. Therefore, it is imperative to discover alternative cement with less CO₂ footprint and dependency on natural resources.

Alkali-activated cements (AAC), with a 20% CO₂ emission of Portland cement, have emerged as a promising alternative to OPC^{9,10}. Beyond addressing CO₂ footprint concerns, these substitutions also provide a more efficient solution to economic and environmental challenges associated with industrial waste disposal¹¹.

The production of AAC involves activating solid aluminosilicates in pozzolanic sources through the application of an alkaline activator solution. During this process, aluminosilicates dissolve in alkaline solutions, and initial gels, called oligomer chains, are created. Over time, the formed gels undergo a transformation,

Department of Civil and Environmental Engineering, Amirkabir University of Technology, Tehran, Iran. ✉email: fattahi.m.s@aut.ac.ir

resulting in the development of longer and denser networks of chains. Ultimately, these chains combine to create a three-dimensional structure of aluminosilicates¹².

The aluminosilicate sources involve industrial by-products like ground granulated blast furnace slag (GGBFS), waste glass powder, as well as natural materials such as metakaolin and volcanic ash^{11,12}. The most available alkaline activating solutions include sodium or potassium hydroxide and sodium silicate, which can be applied individually or in combination, depending on the chemical composition of the utilized aluminosilicate source⁵.

Among aluminosilicate precursors, GGBFS, a byproduct generated during steel production, forms when molten slag from the blast furnace is rapidly cooled, typically with water, creating a highly reactive granular material¹³. It accounts for about 13–20% of total crude steel production and 25–30% of iron ore production¹⁴.

In recent years, numerous investigations have evaluated the utilization of AAC as a stabilizer for clayey soils. De Araújo et al.¹⁵ evaluated clayey soil stabilized with an alkali-activated binder composed of sugarcane bagasse ash, hydrated eggshell lime, and sodium hydroxide as the activator. The study demonstrated unconfined compressive strengths (UCS) of up to 5 MPa and reduced porosity in room-temperature curing conditions. Similarly, Syed et al.¹⁶ investigated the use of steel slag and fly ash with sodium silicate and sodium hydroxide as activators to stabilize expansive soils, reporting a 23–26% increase in subgrade strength compared to cement-treated soils. In another study, Mypati and Saride¹⁷ utilized low-calcium fly ash activated by sodium hydroxide and sodium silicate, achieving a tenfold improvement in UCS and significant reductions in swell-shrink behavior with an optimal binder ratio of 1.5. Additionally, Pourakbar et al.¹⁸ demonstrated the potential of sewage sludge activated by NaOH and Na₂SiO₃ to stabilize clayey soil, achieving UCS improvements from 176 kPa to 1.46 MPa and enhanced Mohr–Coulomb parameters, while reducing metal leachability. These investigations consistently report notable improvements in strength, effective control of swelling, and reduction in the plasticity of the AAC-treated cohesive soils. However, some areas such as long-term performance and cost-effectiveness of AAC stabilization require further study.

In addition to cohesive soils, a growing body of research has examined AAC stabilization of sandy soils. Rios et al.¹⁹ investigated silty sand stabilized with AAC derived from low-calcium fly ash and sodium-based alkaline solutions. Their findings demonstrated significant stiffness and strength improvements, even under wetting and drying cycles, with durability comparable to conventional soil–cement. Similarly, Martins Lima et al.²⁰ examined the effects of ceramic waste and carbide lime as AAC precursors for stabilizing granular soils. Through unconfined compressive strength (UCS) and simple shear testing, they highlighted the role of silica modulus and porosity/binder indices in predicting strength and durability. Moreover, Han et al.²¹ explored the enhancement of coral sand, a weak coastal soil, using alkali-activated slag modified with biochar. The results demonstrated notable increases in strength, elastic modulus, and water retention, although wet-dry cycle resistance slightly decreased at higher biochar contents. Additionally, Disfani et al.²² focused on fine and medium sands treated with alkali-activated fly ash, achieving UCS values exceeding deep-mixing soil stabilization requirements. Kianynejad et al.²³ also explored reinforced AAC systems using metakaolin, calcium carbide residue, and glass wool microfibers, demonstrating improved compressive strength, ductility, and flexural behavior.

Despite these advances, existing research predominantly emphasizes UCS testing, leaving a critical gap in the comprehensive understanding of the triaxial behavior of AAC-treated granular soils. This study aims to thoroughly characterize the mechanical and microstructural properties of loose sandy soil stabilized with alkali-activated GGBFS. To assess the mechanical behavior, samples treated with varying proportions of GGBFS and curing durations were subjected to UCS and CU triaxial tests. The CU tests, conducted under confining pressures of 50, 100, and 150 kPa, were used to evaluate performance under shallow to semi-deep stress conditions. Furthermore, the nature and development of interparticle bonding were examined using FE-SEM, EDX, and FTIR analyses.

Materials and methods

Materials

In the presented study, a silty sand (pH = 9.66, G_s = 2.65, γ_{max} = 18.2, and γ_{min} = 14.3) was utilized as the base material. Moreover, the aluminosilicate precursor for AAC treatment was GGBFS from Isfahan Steel Factory. To prepare the alkaline activator solution, laboratory-grade granular sodium hydroxide (NaOH) with a purity of 99% and a density of 2.13 g/cm³ at 20 °C was used. Figure 1 shows the gradation curve for both soil and GGBFS, and Table 1 presents their chemical composition, determined by XRF analysis. The chemical composition of GGBFS reveals that GGBFS is a calcium-rich aluminosilicate source^{24,25}.

Methods

Specimen preparation

To prepare specimens with a relative density (Dr) of 30%, 133 g and 302 g of silty sand were mixed thoroughly with varying proportions of GGBFS (i.e., 1%, 2%, 4%, and 6% wt.% of soil) for UCS and triaxial tests, respectively. A 2 M NaOH activator solution containing 10% by weight of the soil was then incorporated into the mixtures. Following this, the mixtures were layered using the method proposed by Ladd²⁶ in cylindrical molds. The uniaxial test samples were cast in molds with a diameter of 38 mm and a height of 76 mm, using a three-layer approach, whereas the triaxial test samples were formed in molds with a diameter of 50 mm and a height of 100 mm, employing a five-layer technique. After compacting the soil inside the molds, the samples were removed from the molds, placed in plastic bags, and cured for 7 and 28 days under ambient conditions at 25 ± 2 °C.

The samples treated with alkali-activated GGBFS were indicated by G, followed by a number representing GGBFS content. The curing days and confining pressure in triaxial tests were represented by D and CP, respectively, with the specific value for each parameter shown by the following number. For instance, G6D7CP150 designated

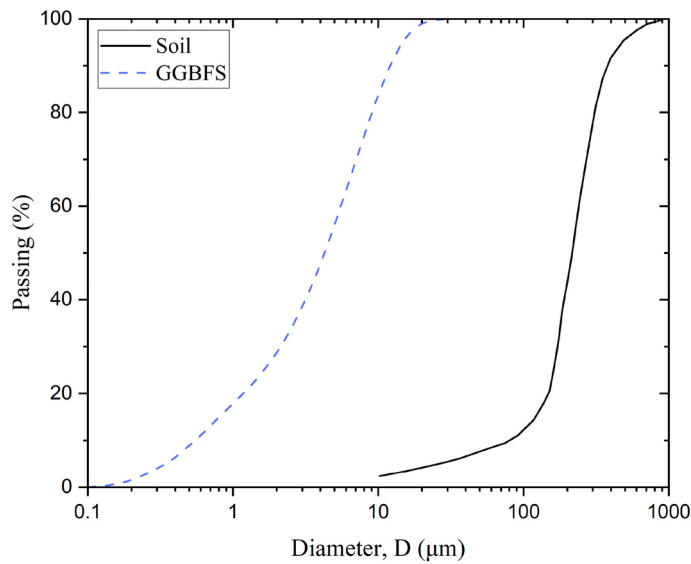


Fig. 1. Gradation curve of soil and GGBFS.

Component [wt%]	CaO	SiO ₂	Al ₂ O ₃	MgO	TiO ₂	MnO	SO ₃	Fe ₂ O ₃	K ₂ O	Na ₂ O	P ₂ O ₅	LOI
Silty sand	1.41	81.89	6.10	0.24	0.79	0.03	–	5.98	0.35	0.51	0.03	2.05
GGBFS	37.90	35.90	8.40	8.90	1.90	1.50	0.90	0.60	0.70	0.70	0.01	0.89

Table 1. XRF analysis results. LOI, loss on ignition.

the sample treated with GGBFS of 6 wt% of soil cured for 7 days and consolidated at 150 kPa confinement. Also, it should be mentioned that samples with zero GGBFS content represent untreated soil.

Uniaxial compressive test

The unconfined strength of the treated samples was assessed according to ASTM.D1633-17²⁷ guidelines. The specimens were loaded at a pace of 1 mm/min, and the stress–strain curve was determined by averaging the results from three tests.

Triaxial compression test

Following the ASTM.D4767-11²⁸, the samples were subjected to CU triaxial tests to assess their mechanical and pore pressure response. The tests were conducted using a computer-controlled triaxial MTM device in strain-control mode at a 1 mm/min strain rate, with constant confining pressure applied during axial loading.

The CU testing consisted of three phases: saturation, consolidation, and shearing. Initially, the sample was subjected to low confinement, and then CO₂ was passed through to accelerate subsequent saturation. Next, de-aired water, at least twice the sample’s volume, was flowed through the specimen. Afterward, incremental back pressure was applied consistently, maintaining a 10 kPa difference from the cell pressure. Once Skempton’s pore pressure parameter (B) reached 0.95 or higher, saturation was confirmed. Following this, the specimen was consolidated under effective confinement pressures of 50 kPa, 100 kPa, and 150 kPa. These pressures were chosen to represent stress conditions typically encountered in semi-deep soil improvement projects. Finally, after the pore pressure dissipated, the sample underwent undrained deviatoric stress until either failure or 20% strain, whichever occurred first.

Finally, after the pore pressure dissipated, the sample underwent undrained deviatoric stress until either failure or 20% strain, whichever occurred first.

In triaxial compression tests, the deviatoric stress (*q*) and mean stress (*p*′) were defined using the following equations:

$$q = \sigma'_1 - \sigma'_3 \tag{1}$$

$$p' = \frac{\sigma'_1 + 2\sigma'_3}{3} \tag{2}$$

where σ'_1 and σ'_3 denotes the effective major and minor stresses respectively.

The secant modulus at 50% of the shear strength (E_{50}) was calculated to evaluate the stiffness of the samples. Moreover, the brittleness index (I_B), as an indicator of the brittle behavior, was calculated by the equation suggested by Consoli et al.²⁹:

$$I_B = \frac{q_{max}}{q_{res}} - 1 \quad (3)$$

where q_{max} and q_{res} are the peak and residual deviatoric stresses, respectively.

The energy absorption capacity, which indicates the energy required to deform the samples, was assessed by calculating the area under the stress–strain curve. To ensure consistency in comparative analyses, energy absorption in this study was calculated at an axial strain of 10% ($E_{D,10\%}$). This approach avoids bias towards brittle or ductile behavior, ensuring accurate reflections of practical soil performance.

The peak deviatoric stress criterion was used to calculate the undrained strength parameters for the treated samples and both the undrained and drained parameters for the untreated soil. Determining effective strength parameters from undrained triaxial tests presents significant challenges for highly dilative samples, which tend to expand markedly under deviatoric stress. This study adopts the methodology of Baxter et al.³⁰ to determine the failure envelope for such samples. This method is particularly suited to the tested soils, as it mitigates the impact of significant negative pore pressure generated by high dilation tendencies. Negative pore pressure in dilative soils can increase the apparent shear strength under undrained conditions, leading to overestimated effective strength parameters. By applying the zero excess pore pressure ($\Delta u = 0$) criterion at failure, the Baxter methodology minimizes this effect, providing a more accurate representation of the drained strength parameters. However, it should be noted that the $\Delta u = 0$ criterion is particularly suitable for soils with uniform properties, where the transition from contraction to dilation occurs consistently. However, in soils with variable cementation or heterogeneity, this transition may be uneven, potentially limiting the applicability of the criterion.

Skempton's equation for excess pore pressure occurring under changes in the principal stresses $\Delta\sigma_1$ and $\Delta\sigma_3$ are given by the following equation:

$$\Delta u = B [\Delta\sigma_3 + A (\Delta\sigma_1 - \Delta\sigma_3)] \quad (4)$$

where A and B are pore-pressure parameters. For the conventional compression triaxial test, the equation is simplified as follows in applying the deviatoric stress stage:

$$\Delta u = \bar{A} \Delta\sigma_d \quad (5)$$

where $\bar{A} = A/B$ and $\Delta\sigma_d$ represents changes in deviatoric stress. Following Baxter et al.³⁰, when the \bar{A} coefficient is set to zero, Δu corresponding to sample failure equates to zero, and substantial negative pore pressure is disregarded. Consequently, the principal stresses corresponding to $\Delta u = 0$ are employed to establish drained failure envelopes and shear strength parameters.

Microstructural tests

The field emission scanning electron microscope (FE-SEM) and energy-dispersive X-ray spectroscopy (EDX) of MIRA3, TESCAN Co., were utilized to examine the surface morphology and the formation of alkali-activated GGBFS in the treated samples, respectively. Additionally, an FTIR Thermo Nicolet Avatar 380 series spectrometer was used to evaluate the functional groups and bonds formed in the samples with varying GGBFS content.

Statistical analysis

In this study, ORIGIN PRO 2022 software was used for statistical analysis. Regression analysis was utilized to determine the correlations between GGBFS content and various properties, including brittleness index, failure deviatoric stress, failure axial strain, secant modulus at 50% of shear strength, absorbed energy, friction angle, and cohesion. Additionally, linear correlations were established between deviatoric stress and mean effective stress to derive failure envelopes. Moreover, cohesion parameters were correlated with the maximum stress of the UCS samples, and the significance of these relationships was evaluated using the F-test.

Results

Uniaxial compressive test

Figure 2 depicts the stress–strain curve obtained from uniaxial compressive tests performed on the samples treated with varying GGBFS content after 7 and 28 days of curing. Notably, the untreated soil could not undergo this test due to its lack of cohesion and subsequent instability. The results show a progressive increase in compressive strength with higher GGBFS content, with the maximum strength observed for samples containing 6% GGBFS. Additionally, the curing duration significantly affects the mechanical response, with samples cured for 28 days exhibiting higher strength and stiffness compared to those cured for 7 days. The stress–strain behavior also transitions from ductile to brittle as the GGBFS content increases, evident from the sharper post-peak stress drops in samples with higher GGBFS percentages.

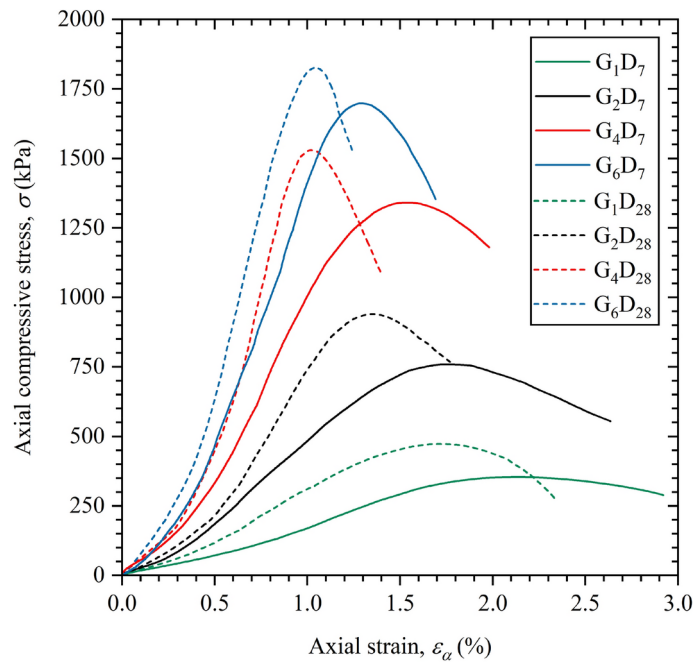


Fig. 2. Stress–strain curve based on uniaxial compressive test of treated soil using alkali-activated GGBFS with varying contents after 7 and 28 days of curing.

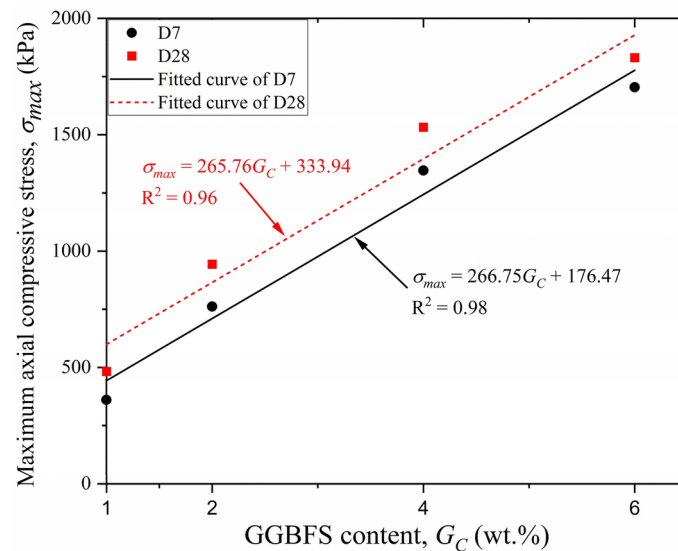


Fig. 3. Correlation of maximum axial compressive stress with GGBFS content and curing time.

Figure 3 depicts the relationship between maximum axial compressive stress (σ_{max}) and GGBFS content (G_C) for samples cured for 7 and 28 days. The maximum axial stress increases consistently with higher GGBFS content, following a linear trend as represented by the equations.

$\sigma_{max} = 266.75G_C + 176.47$ for 7 days cured samples and $\sigma_{max} = 265.76G_C + 333.94$ for 28 days cured samples. No evidence of a saturation effect is observed, as σ_{max} continues to rise linearly with increasing GGBFS content across the tested range.

Figure 4 illustrates the relationship between axial strain at maximum stress (ε_{max}) and GGBFS content (G_C) for samples cured for 7 and 28 days. The axial strain decreases consistently with higher GGBFS content, following a power-law trend described by the general formula $\varepsilon_{max} = aG_C^b$, where a and b are fitting coefficients. The results also indicate that curing time has a noticeable impact on axial strain, with samples cured for 28 days exhibiting slightly lower axial strain values at maximum stress compared to those cured for 7 days.

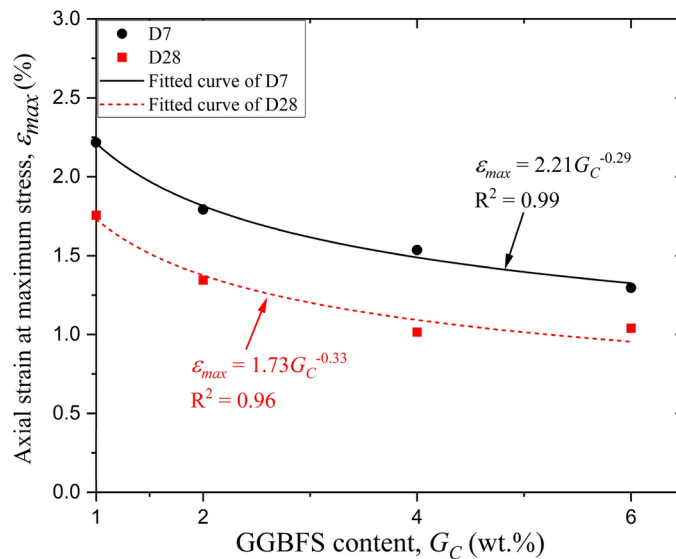


Fig. 4. Correlation of axial strain at maximum stress with GGBFS content and curing time.

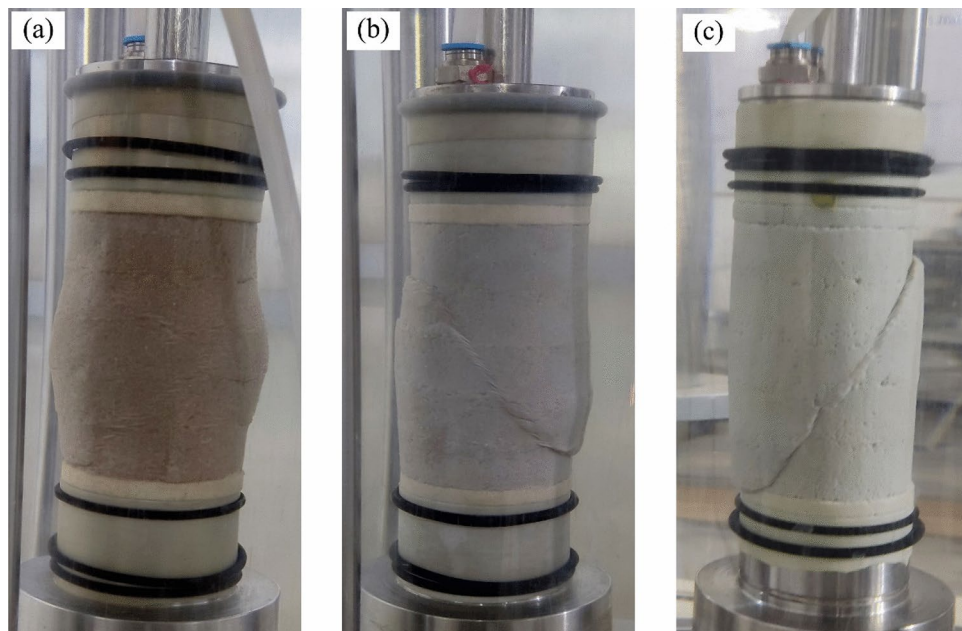


Fig. 5. Failure modes of tested samples: (a) barreling mode in G1D7CP100 sample (b) shear zone failure of G4D28CP100 sample (c) shear zone failure of G6D28CP100 sample.

Triaxial test results

Typical failure modes of the samples

Figure 5 illustrates the typical failure modes observed in the tested samples under undrained conditions. All untreated soil samples exhibited a barreling mode with no distinct shear plane formation. Additionally, in samples with low GGBFS content and high ductility (i.e., G1 and G2), barreling was the predominant failure mode, as shown in Fig. 5a. However, with the rise in GGBFS content, the failure mode markedly changed, and a well-defined shear band became apparent. When comparing Fig. 5b,c, it is evident that samples with a higher GGBFS content displayed distinct shear bands.

Stress–strain and pore water pressure response

Figure 6 demonstrates the q and Δu versus axial strain (ϵ_a) for the samples in the triaxial tests. These experiments were conducted under varying GGBFS contents, confinements, and curing periods.

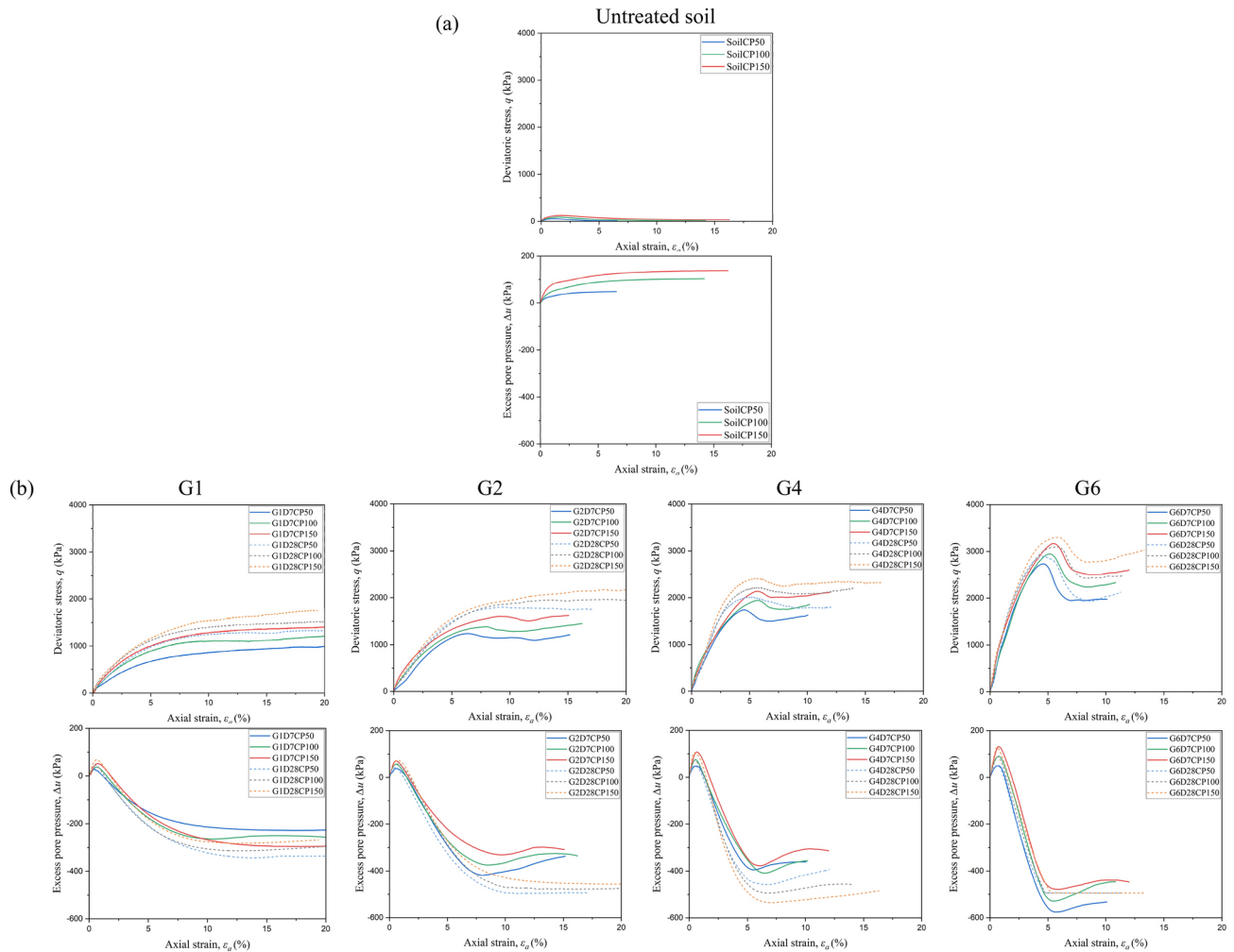


Fig. 6. Undrained triaxial behavior; $q - \varepsilon_a$ and $\Delta u - \varepsilon_a$ curves: (a) untreated samples (b) treated samples.

In considering $q - \varepsilon_a$ curves, the majority of the samples exhibited a strain-softening response, indicative of brittle behavior. However, the G1D7s, G1D28s, G2D28CP100, and G2D28CP150 samples demonstrated a strain-hardening response, representing ductile behavior. Upon comparing the $q - \varepsilon_a$ curves of the treated samples with the untreated samples, a notable enhancement in strength was observed.

As shown in Fig. 6b, the increase in GGBFS content (G_c), cell pressure, and curing time corresponded to a rise in deviatoric stress at failure (q_f) and a stiffer behavior. Additionally, the augmentation of G_c resulted in a lower axial strain at failure (ε_f), and a greater difference between maximum and residual deviatoric stresses. However, unlike the effect of GGBFS content, an increase in cell pressure and curing time resulted in less difference between maximum and residual deviatoric stresses and greater ductility. Moreover, higher GGBFS content, increased cell pressure, and extended curing time resulted in a larger energy absorption.

Regarding the $\Delta u - \varepsilon_a$ curves, due to the loose condition (D_r of 30%) of the untreated sample, its pore pressure increased until reaching a constant value, and its contraction tendency increased as the cell pressure increased. However, treated samples initially displayed a contractive tendency at low strains, followed by a rapid decrease, signifying a notable inclination toward dilation. Additionally, positive pore pressure at low ε_a , as well as the absolute magnitude of negative pore pressure associated with dilation tendencies, increased with higher levels of cementation. According to Fig. 6b, the Δu of the G6D7CP50 sample reached -576 kPa after a significant reduction, representing the maximum absolute value of measured negative pore pressure. Furthermore, the negative pore pressure corresponding to G6D28 samples was not fully measured due to sensor limitations in the triaxial test device.

As confinement increased, the tendency of the samples to dilate generally decreased, except for the cases of G1D7 and G4D28, where the opposite trend was observed. This opposite trend indicates uncertainty in the magnitude of negative pore pressure at high strains. Furthermore, the dilation tendency was more pronounced in 28 days cured samples compared to 7 days cured ones.

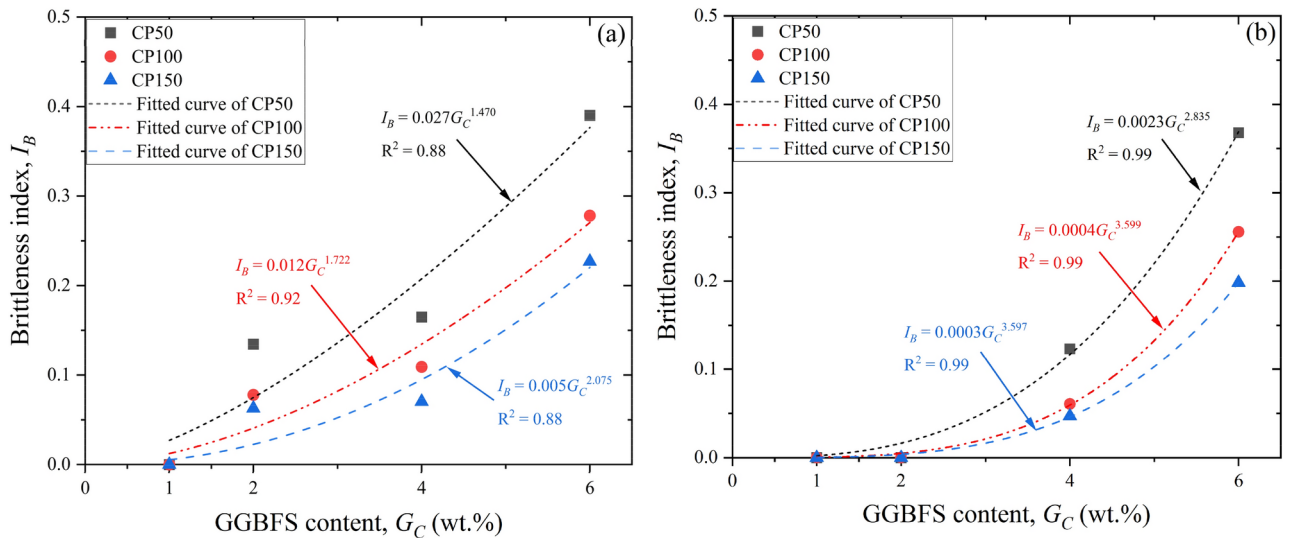


Fig. 7. Correlation of I_B with GGBFS content and confinement: samples cured for (a) 7 days, (b) 28 days.

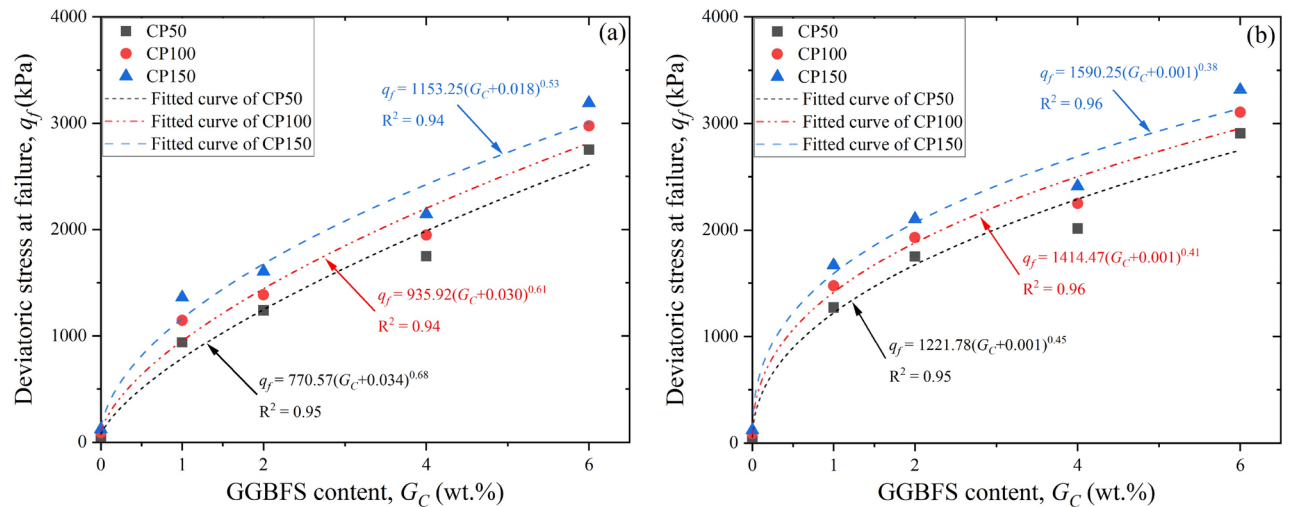


Fig. 8. Correlation of q_f with GGBFS content and confinement: samples cured for (a) 7 days, (b) 28 days.

Relationship between brittle index (I_B) and GGBFS content (G_C)

Figure 7 illustrates the relationship between I_B and G_C at various confinements and curing times for the treated samples. Given that the untreated samples displayed negligible residual strengths (see Fig. 6a), the calculation of the I_B was exclusively performed for the treated samples.

According to Fig. 7, the fitted curves exhibited a robust power relationship between I_B and G_C characterized by the general equation of $I_B = a \times G_C^b$. The coefficients a and b were obtained via fitting curves. I_B increased with higher GGBFS content. For instance, under a confining pressure of 100 kPa, G6D7 and G6D28 samples exhibited I_B values of 0.28 and 0.26, respectively, while G1 samples displayed ductile behavior, with $I_B = 0$.

Furthermore, as the confinement increases, I_B decreases. For example, I_B values for G6CP50, G6CP100, and G6CP150 samples after 7 days of curing were 0.39, 0.28, and 0.23, respectively. Comparing Fig. 7a,b, it is evident that the I_B of samples cured for 28 days was lower than that of samples cured for 7 days. Additionally, a transitional behavior was observed in the G2 samples over the curing period. While G2D7 samples exhibited a slight post-peak strain-softening behavior, G2D28 samples demonstrated ductile behavior, with $I_B = 0$.

Relationship between deviatoric stress at failure (q_f) and GGBFS content (G_C)

The relationship between q_f and G_C under varying confinements and curing times is presented in Fig. 8. The failure points of all specimens were determined from their stress–strain behavior. For strain-softening specimens, the failure point was identified at the peak deviatoric stress, while for strain-hardening specimens, it was defined at 15% axial strain in accordance with ASTM.D4767-11²⁸.

As shown in Fig. 8, a strong relationship ($R^2 \sim 0.95$) between q_f and G_C was revealed by the fitted curves, with the general equation of $q_f = a(G_C - b)^c$. An increase in G_C corresponded to an increase in q_f . Notably, a mere 1% GGBFS addition resulted in a substantial strength difference between G1 and untreated samples. For instance, the q_f of G1D7 and G1D28 at a confinement of 100 kPa increased by 12 and 16 times, respectively, compared to untreated samples.

Additionally, it is evident that greater confinement leads to an increase in q_f , as expected. Comparing Fig. 8a and b reveals that the shear strength of samples cured for 28 days exceeded that of samples cured for 7 days. Nonetheless, there was a slight disparity in shear strength between the 7 day and 28 day cured of G4 and G6 samples.

Relationship between failure axial strain (ε_f) and GGBFS content (G_C)

Figure 9 displays the relationship between ε_f and G_C under varying confinements and curing times. The fitted curves illustrated a peak-shaped correlation between ε_f and GGBFS content with a general equation of $\varepsilon_f = a + b \exp(-\exp(-z) - z + 1)$, where $z = c(G_C - d)$. Here, a, b, c, and d are fitting coefficients obtained from regression analysis. The term $z = c(G_C - d)$ introduces a scaling and shifting factor that determines the peak position of the fitted curve.

Additionally, the dashed horizontal lines at 15% axial strain mark the upper limit of axial strain at failure, following the guidelines in ASTM.D4767-11²⁸.

As shown in Fig. 9, a notable difference in ε_f was evident between the untreated samples and G1 samples. As shown in Fig. 6a,b, the stress-strain curves of untreated specimens exhibited a distinct peak corresponding to failure at approximately 1.5% strain, while the G1 samples displayed a completely ductile behavior up to a strain of 20%. In Fig. 9a,b, peaks in the fitted curves occurred at approximately 1% and 1.5% GGBFS content, respectively. Subsequently, as the GGBFS content increased, ε_f decreased; however, there was a negligible difference in ε_f between the G4 and G6 samples.

According to Fig. 9, varying confinements have little impact on ε_f especially in the 28-day cured samples (Fig. 9b), where differences were not discernible. Moreover, when comparing Fig. 9a,b, it becomes evident that substantial differences in ε_f existed between the G2D7 and G2D28 samples. This indicates the transitional behavior over curing time as mentioned previously.

Stiffness of the samples

Figure 10 illustrates the change of secant modulus (E_{50}) with G_C under different confinement levels for both 7 days and 28 days treated samples. The fitted curves demonstrated that E_{50} increased with G_C with a strong relationship described by the general equation of $E_{50} = a + bG_C^c$, where a and b were obtained from the fitted curves.

A comparison between Fig. 10a,b indicates an increase in E_{50} with extending curing time. However, the positive influence of confinement in increasing E_{50} diminished as curing time increased. In essence, the impact of confinement on the E_{50} of the 28 days cured samples was not remarkable.

Energy absorption

Figure 11 illustrates the correlation between the energy absorption capacity of the samples at an axial strain of 10% ($E_{D,10\%}$) and G_C under various confinement levels for both 7-day and 28-day treated samples. The variables $E_{D,10\%}$ and G_C demonstrated a highly correlated relationship ($R^2 > 0.95$), characterized by the equation $E_{D,10\%} = a(G_C + b)^c$, where a, b, and c represent the associated parameters.

As shown in Fig. 11, an increase in GGBFS content, cell pressure, and curing time corresponded to a rise in $E_{D,10\%}$. Notably, a substantial difference in $E_{D,10\%}$ was observed between untreated soil and G1 samples containing

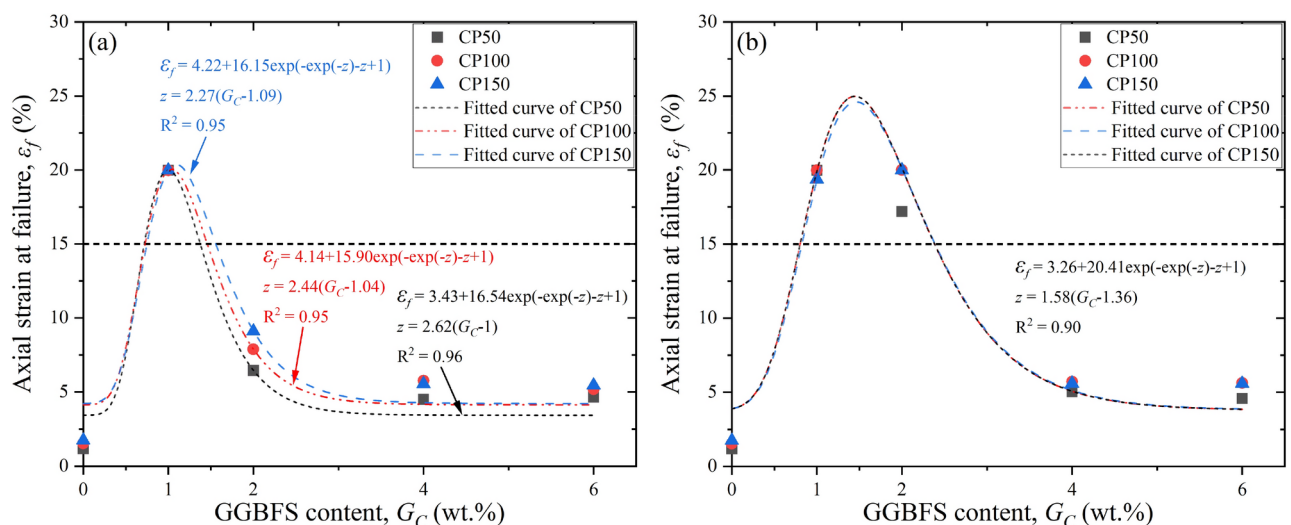


Fig. 9. Correlation of ε_f with GGBFS content and confinement: samples cured for (a) 7 days, (b) 28 days.

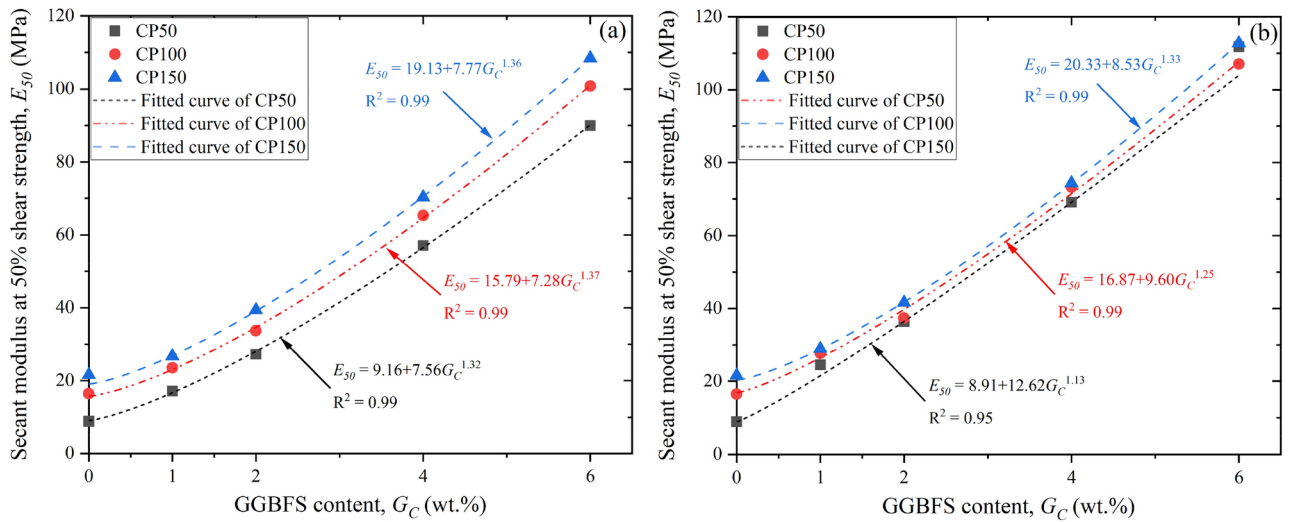


Fig. 10. Correlation of E_{50} with GGBFS content and confinement: samples cured for (a) 7 days, (b) 28 days.

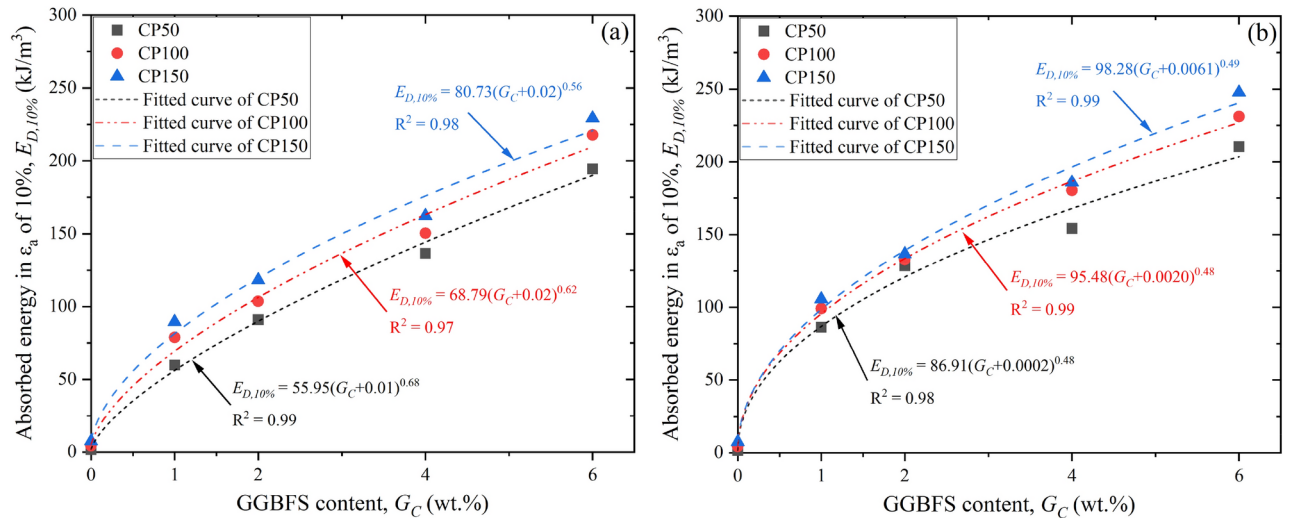


Fig. 11. Correlation of $E_{D,10\%}$ with GGBFS content and confinement: samples cured for (a) 7 days, (b) 28 days.

only 1% GGBFS. For Instance, the $E_{D,10\%}$ value of the G1D28 sample under a 150 kPa confinement was 13.1 times greater than the corresponding untreated sample.

Failure envelopes and shear strength parameters

Figure 12 presents the drained failure envelopes for all tests conducted at both 7 days and 28 days curing times. Additionally, Figs. 13 and 14 show the variation of friction angle (ϕ and ϕ') and cohesion (C and C') with GGBFS content.

As shown in Fig. 13, the treated samples with alkali-activated GGBFS exhibited a nearly constant internal friction angle with increasing GGBFS content under both drained and undrained conditions, with minimal influence from curing time. Conversely, cohesion increased with GGBFS content and curing time as depicted in Fig. 14. It is also noteworthy that ϕ' and C' were lower than the respective undrained values.

The relationship between triaxial test results and uniaxial compressive test

To compare undrained and drained cohesion parameters resulting from soil stabilization with alkali-activated GGBFS, a correlation between these two parameters and UCS was established. Figure 15 illustrates this correlation, demonstrating a linear function, where C and C' are approximately 0.3 and 0.1 of UCS, respectively.

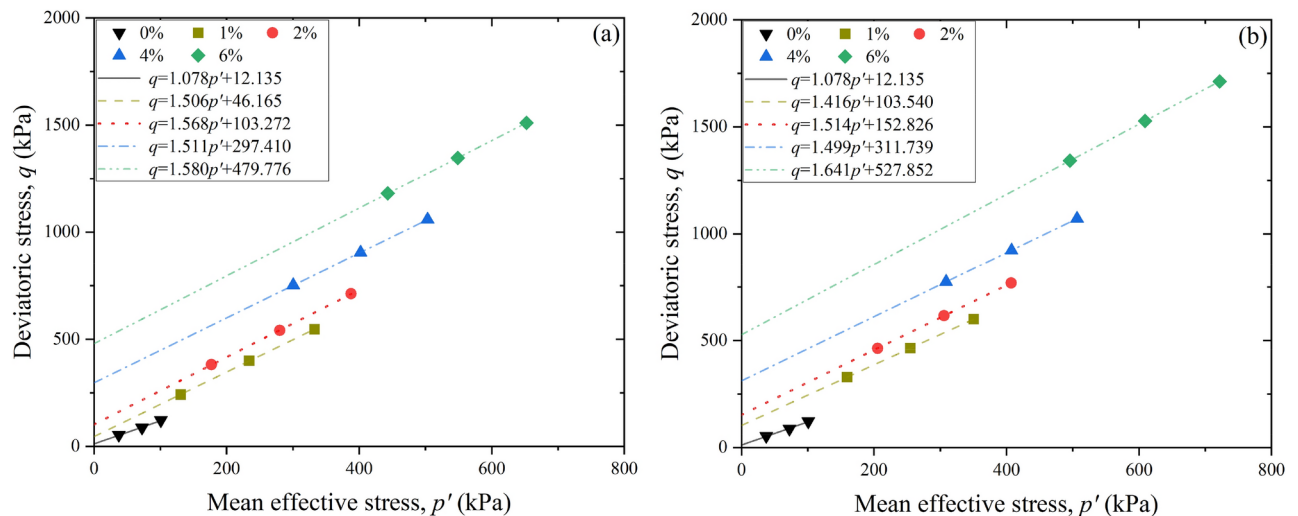


Fig. 12. Drained failure envelopes for the tested samples: samples cured for (a) 7 days, (b) 28 days.

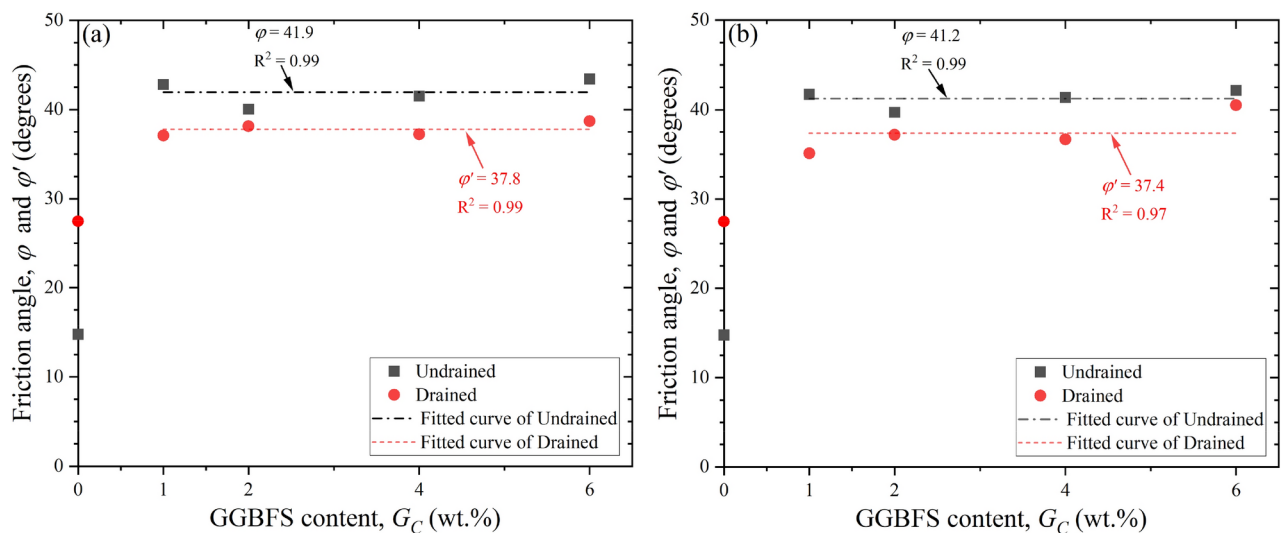


Fig. 13. Correlation of friction angle (ϕ and ϕ') with GGBFS content: samples cured for (a) 7 days, (b) 28 days.

Microstructural analyses

FE-SEM and EDX analysis

Figure 16 illustrates the FE-SEM and EDX analyses performed on the GGBFS-treated samples after 28 days of curing. The FE-SEM images provide a magnified view of 10,000X, revealing the formation of gels throughout the alkali-activation process of GGBFS. These images reveal the formation of calcium-silicate-hydrate (C-S-H), sodium-aluminosilicate-hydrate (N-A-S-H), calcium-aluminosilicate-hydrate (C-A-S-H), and a combination of N-A-S-H and C-A-S-H, collectively referred to as (N, C) A-S-H gels. Based on prior studies conducted by researchers such as Kamath et al.³¹, Li et al.³², and Provis et al.³³, the specific appearances of these gels were identified: C-S-H gels exhibited fibrous or layered structures, C-A-S-H gels displayed plate-like or irregular morphologies, and N-A-S-H gels presented an amorphous and loosely packed structure.

The EDX analyses further support these findings by confirming the elemental composition of the observed gels, with silicon (Si), oxygen (O), calcium (Ca), aluminum (Al), and sodium (Na) identified as the major elements. For instance, the EDX spectrum of the G6D28 sample reveals a composition of 38.55% Si, 33.90% O, 11.21% Ca, and 7.24% Al by weight, confirming the formation of N-A-S-H and C-A-S-H gels.

FTIR analysis

Figure 17 illustrates the outcomes of FTIR analysis performed on both untreated and treated soil with varying GGBFS content after 28 days of curing, within the wave number range of 450–4000 cm^{-1} .

Broadly, the bonds observed within the 450–1100 cm^{-1} range were associated with aluminosilicate bonds in the N-A-S-H and C-A-S-H phases. In this investigation, the GGBFS-treated sample displayed multiple

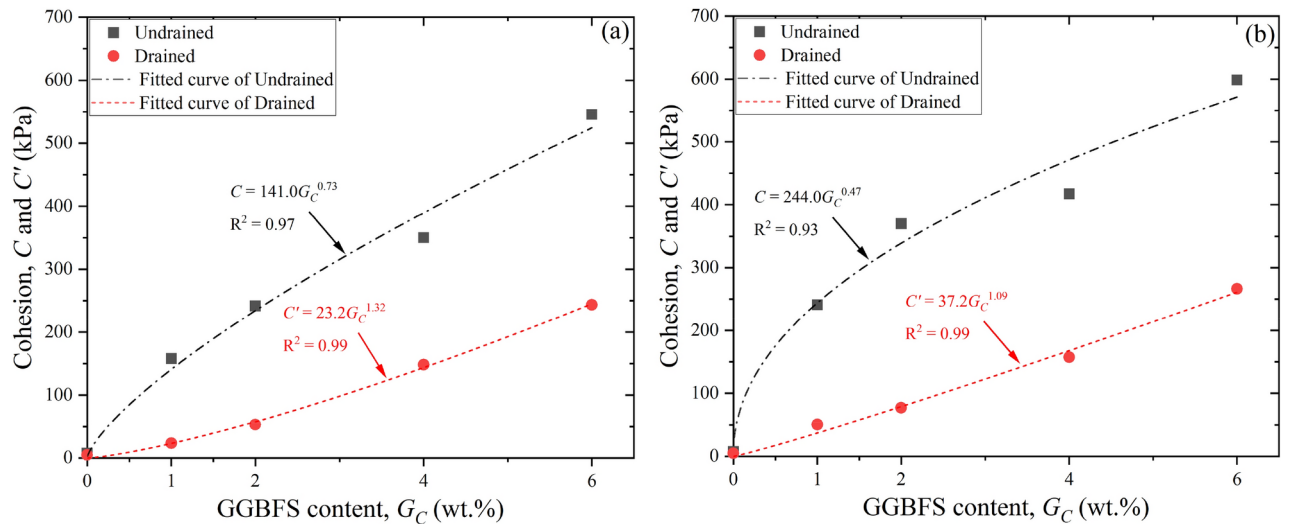


Fig. 14. Correlation of cohesion C and C' with GGBFS content: samples cured for (a) 7 days, (b) 28 days.

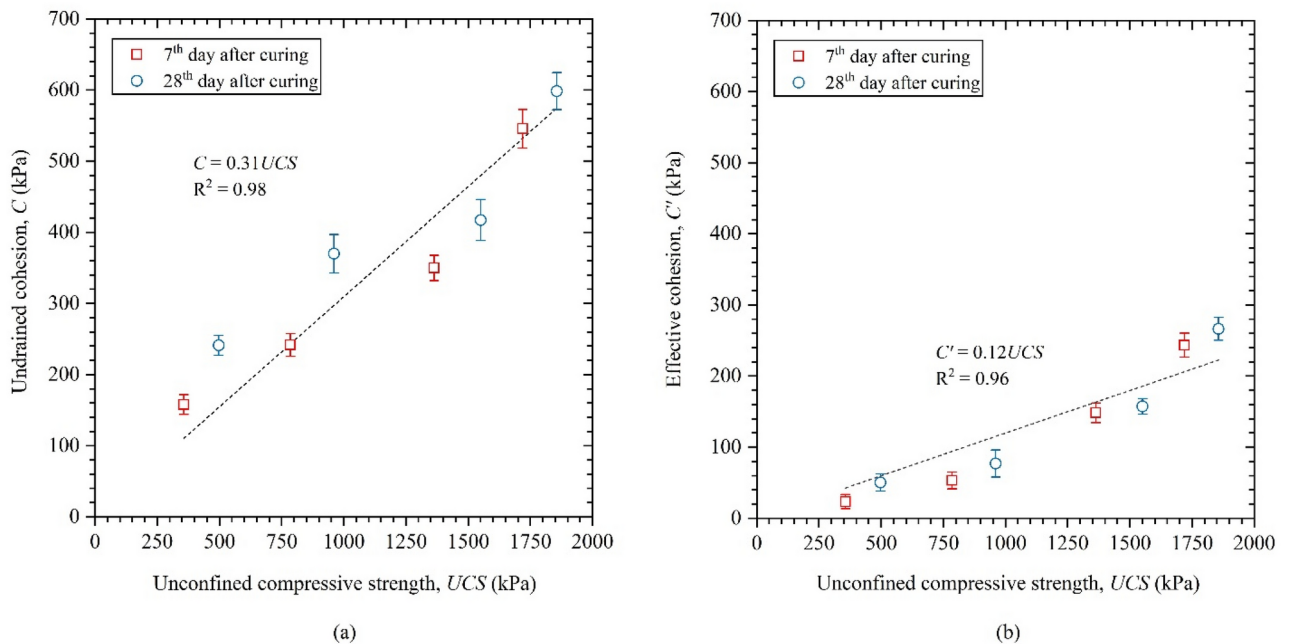


Fig. 15. The correlation between cohesion (C and C') and UCS of the treated samples with varying GGBFS content after 7 and 28 days of curing.

bonds within this range. As the GGBFS content increased, the peaks in these bonds became more prominent, suggesting enhanced bond strength, accompanied by a corresponding decrease in transmittance percentage.

Bonds in the $1400\text{--}1440\text{ cm}^{-1}$ range were associated with carbonates formed from the reaction between alkali hydroxides in AAC and atmospheric CO_2 . Peaks in the $1500\text{--}1700\text{ cm}^{-1}$ range corresponded to crystalline water, while those in the $3000\text{--}3500\text{ cm}^{-1}$ range indicated the presence of water in the voids of the cementation. According to the FTIR findings, as GGBFS content increased, the presence of water between pores and soil particles diminished. This decrease in physical water content has consequently led to an increase in transmittance at this wave number. According to a study by Li et al.³⁴, the O–H bond detected at $3000\text{--}3500\text{ cm}^{-1}$ can be linked to the C–S–H gel.

Discussion

Microstructure of the treated soil

In this study, GGBFS and NaOH solution were employed as the aluminosilicate precursor and activating agent, respectively, to stabilize silty sand soil and enhance its mechanical properties. The presence of C–S–H, N–A–

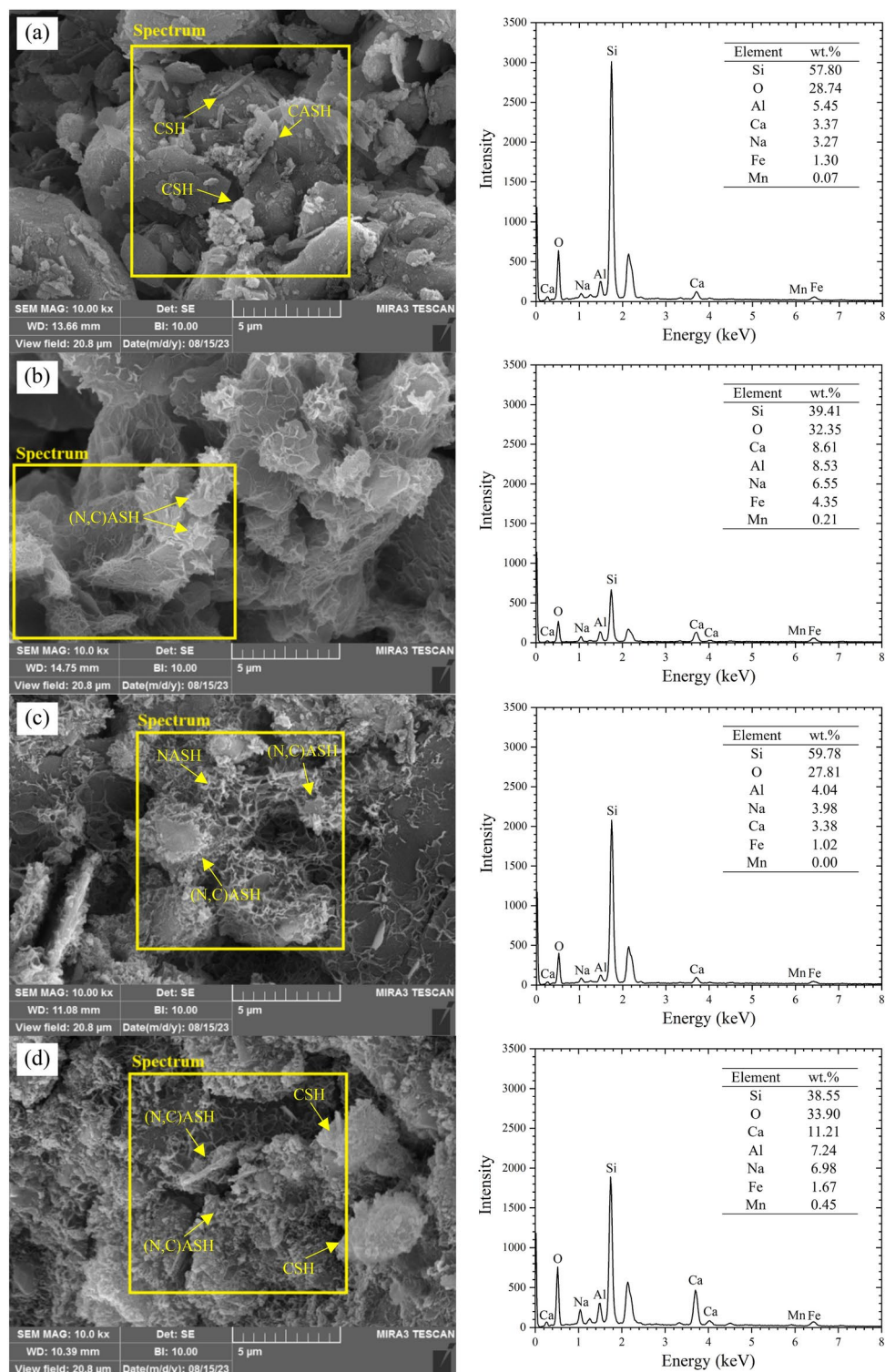


Fig. 16. FE-SEM and EDX analysis: (a) G1D28 (b) G2D28 (c) G4D28 (d) G6D28.

S-H, C-A-S-H, and (N, C)A-S-H gels, which contribute to interparticle bonding, was confirmed through FE-SEM imaging and EDX analysis. These findings are consistent with earlier research on the microstructure of soils stabilized with AAC^{14,35,36}. The formation of these gels plays a critical role in improving soil properties, as they fill voids and create strong interparticle bonds.

The alkali-activation process, which governs gel formation, begins with the dissolution of calcium-rich aluminosilicates in GGBFS under the highly alkaline conditions provided by NaOH. This dissolution releases reactive ions such as calcium (Ca^{2+}), aluminum (Al^{3+}), and silicon (Si^{4+}), which polymerize to form C-S-H,

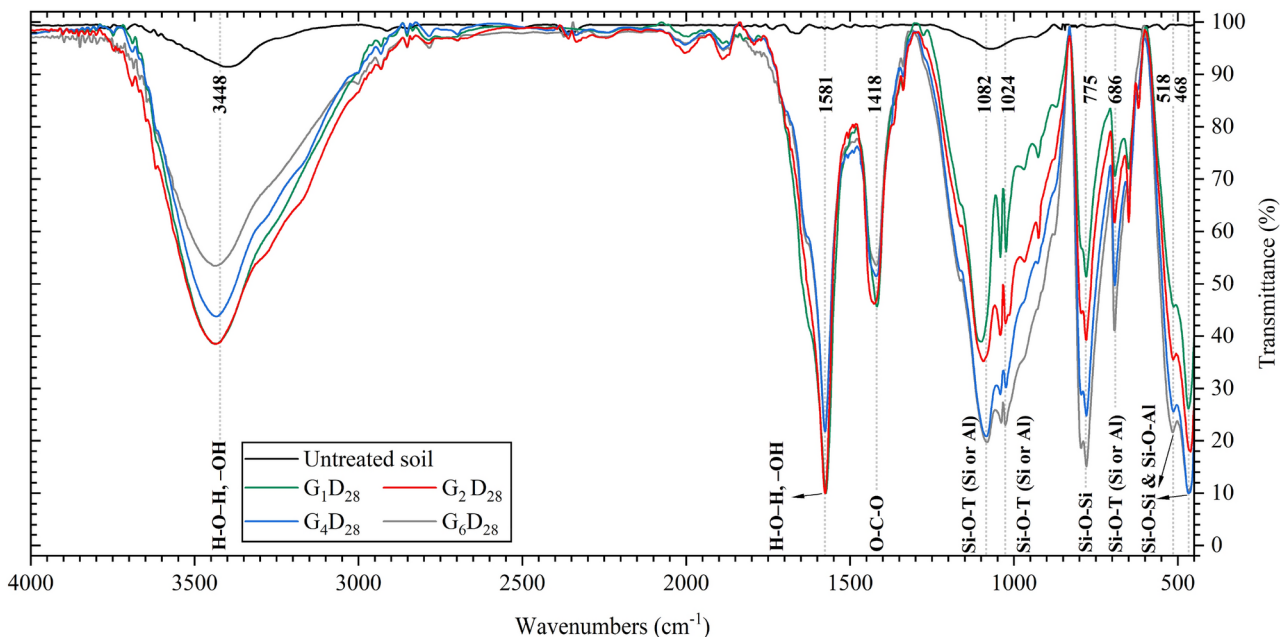


Fig. 17. FTIR analysis results for untreated and treated soil with varying GGBFS content after 28 days of curing.

N-A-S-H, and C-A-S-H gels. The amount of GGBFS directly influences this process, as higher GGBFS content increases the availability of these ions, enhancing gel density and connectivity. This enhancement leads to the formation of a more continuous and robust gel network, transitioning from dispersed clusters in low-GGBFS samples to a dense, uniform matrix in high-GGBFS samples, as shown in Fig. 16.

FTIR analysis complements these findings by revealing the chemical bonds that support gel formation. Bonds identified within the 450–1100 cm^{-1} range, associated with aluminosilicate structures in N-A-S-H, C-A-S-H, and (N,C)-A-S-H gels, become more pronounced with increased GGBFS content^{37,38}. This is evident from the deeper peaks and reduced transmittance percentage observed in FTIR spectra, reflecting a higher density of amorphous gels (Fig. 17). Furthermore, in alignment with prior research, the OH bond occurring between 3000 and 3500 cm^{-1} can be linked to the CSH bond^{34,39}. These changes are consistent with the observed improvements in gel network connectivity and mechanical properties.

Additionally, FTIR analysis reveals that increasing GGBFS content reduces the water present between soil particles, leading to higher transmittance at specific wave numbers. This reduction is primarily attributed to hydration reactions during alkali activation, where free water is consumed in the formation of cementitious gels. Additionally, these gels occupy the pore spaces between soil particles, densifying the soil matrix and limiting its water retention capacity. Consequently, the diminished water content results in less infrared light absorption, explaining the increased transmittance.

Mechanical and pore pressure behavior of treated soil

Brittleness

As shown in Fig. 7, increasing GGBFS content correlates with higher I_B , indicating more brittle behavior, which is consistent with previous studies. This aligns with the failure modes in Fig. 5, where a transition from barreling to distinct shear banding occurs with increased GGBFS content. This transition is linked to changes in the soil's microstructure. At higher GGBFS content, strong bonds between soil particles create a denser and more rigid matrix that restricts particle movement. This rigidity reduces the ability to dissipate energy effectively, causing stress to concentrate in localized regions and ultimately leading to sudden failure along shear bands. Consequently, the breakdown of strong interparticle bonds leads to a sharp drop in stress after peak failure, resulting in a higher brittle index.

Deviatoric stress at failure

As depicted in Figs. 3 and 7, increasing GGBFS content corresponded to higher q_f . This finding aligned with the evidence provided by FE-SEM images and FTIR analyses (Figs. 16 and 17), indicating the enhanced formation of binding gels between particles^{40,41}.

Furthermore, samples cured for 28 days demonstrated superior shear strength compared to those cured for 7 days; however, the influence of the curing period diminished as the GGBFS content increased. This behavior can be attributed to the accelerated pozzolanic reactions at higher GGBFS levels, which facilitate rapid initial strength development⁴². The reduced reliance on extended curing time in high GGBFS-treated soils offers practical advantages, including expedited project timelines and cost efficiencies. Nevertheless, careful

optimization of GGBFS content and curing duration is critical to prevent excessive brittleness, particularly under low-confinement conditions.

Deformability and stiffness

The observed stiffness and deformability behavior of the GGBFS-treated soils demonstrates an inverse relationship between these properties. As shown in Fig. 10, the secant modulus (E_{50}) increased with higher GGBFS content, indicating enhanced stiffness. Conversely, Fig. 4 and Fig. 9 illustrate a reduction in the strain at failure (ϵ_f) with increasing GGBFS content, reflecting diminished deformability. This trend can be attributed to the formation of a denser and more rigid soil matrix as GGBFS content increases, as demonstrated in FE-SEM and FTIR analyses (Figs. 16 and 17). These findings align with the behavior of cemented soils reported in previous studies^{43,44}.

Additionally, Fig. 9 illustrates that E_{50} increased over curing time. However, with increasing confinement, the influence of curing time on E_{50} enhancement diminished. This observation was attributed to the increased confinement, enhancing forces, and particle interactions. Consequently, the impact of curing time on stiffness decreases since the dominant factor influencing stiffness becomes the interparticle forces instead of cementation development during curing time⁴⁵.

Excess pore pressure

In Fig. 6, for GGBFS-treated samples, the excess pore pressure response exhibited an initial tendency for contraction at low strains, followed by a sharp decrease, indicating a significant tendency to dilation. This behavior has been reported in prior studies involving CU triaxial tests conducted on cemented sandy soil^{30,46,47}.

According to Fig. 6b, an increase in cementation content led to a rise in excess pore pressure at low strains and negative suction at high strains. Additionally, with a rise in the cementation level, the transition from positive to negative pore pressure became more pronounced. Similar findings have been reported by Baxter et al.³⁰.

Moreover, an increase in confinement generally resulted in a decrease in negative suction at the end of the loading process, a finding reported similarly by Amini and Hamidi⁴⁶. However, this pattern was not evident in the G1D7 and G4D28 samples, where an opposite trend was observed. This divergent trend aligns with the observations made by Baxter et al.³⁷, indicating variability in pore pressure response at high strains was a consequence of cavitation. When pore pressure decreases during shearing, air trapped in the pore water starts to escape once it falls below a certain level. As a result, this influences the pore pressure response, which causes significant uncertainty in determining effective strength parameters.

Strength envelope and parameters

In this study, $\Delta u = 0$ criterion recommended by Baxter et al.³⁰ was used to establish drained strength envelopes and their associated parameters, as depicted in Figs. 12, 13, and 14. As illustrated in Fig. 14, higher GGBFS content and longer curing time result in increased cohesion, consequently enhancing shear strength (Fig. 6). Additionally, the increase in cohesion as a result of higher GGBFS content is evident in the FE-SEM and FTIR analyses, presented in Figs. 16 and 17, respectively. However, as depicted in Fig. 13, the internal friction angle remains relatively constant across all conditions, aligning closely with the results presented by Amini and Hamidi⁴⁶. This nearly constant internal friction angle observed in GGBFS-treated soils may be attributed to the preservation of the granular structure of particles, which is a key factor influencing frictional behavior. Unlike conventional stabilization methods that alter the arrangement of soil particles through increased cementation, the alkali-activated GGBFS treatment primarily enhances bonding at particle interfaces without significantly modifying the overall granular structure. However, further research is recommended to validate these hypotheses and provide deeper insights into the observed behavior.

Also, the undrained strength parameters of the treated soil were calculated using the peak deviatoric stress criterion. As shown in Figs. 13 and 14, the drained strength parameters, especially the cohesion intercept, were lower than the corresponding undrained values, indicating that the $\Delta u = 0$ criteria effectively eliminated the influence of large negative pore pressure on shear strength⁴⁶.

Furthermore, the linear correlation between the cohesion parameters and UCS was established (Fig. 15). Given the significance and accuracy of the established relationship and the cost-effectiveness and simplicity of conducting the uniaxial test compared to the triaxial test; it can be concluded that utilizing uniaxial tests instead of triaxial tests enables the estimation of the shear strength parameters for the silty sand stabilized with alkali-activated GGBFS.

Conclusion

This study aims to thoroughly evaluate the mechanical and microstructural characteristics of loose sandy soil treated with alkali-activated GGBFS, providing valuable implications for projects involving semi-deep soil stabilization. The findings of this study are summarized as follows:

Microstructural analyses using FE-SEM and EDX revealed the formation of calcium-silicate-hydrate (C-S-H), sodium-aluminosilicate-hydrate (N-A-S-H), calcium-aluminosilicate-hydrate (C-A-S-H), and combined (N, C)-A-S-H gels during the alkali activation process of GGBFS. These gels played a pivotal role in enhancing mechanical properties. Complementary FTIR analysis confirmed the formation and increased density of these gels, corresponding to the higher GGBFS content.

GGBFS-treated soils demonstrated that even with limited GGBFS content (1–6%), the treated samples exhibited significant improvements in strength, stiffness, and energy absorption, underscoring the efficiency of alkali-activated GGBFS as a stabilizer for granular soils. Additionally, samples subjected to a 28 days curing period exhibited greater shear strength and stiffness compared to those cured for 7 days. However, the impact of the curing period became less pronounced with higher GGBFS content.

The increased GGBFS content significantly improved soil cohesion, ranging from 240 to 600 kPa under undrained conditions and 50–270 kPa under drained conditions after a 28 days curing period. However, the internal friction angle remained nearly constant, approximately $42 \pm 2^\circ$ for undrained conditions and $38 \pm 3^\circ$ for drained conditions.

A strong linear correlation between the uniaxial compressive strength (UCS) and the cohesion of stabilized sandy soil treated with alkali-activated GGBFS was established, offering a cost-effective method for estimating shear strength parameters without the need for triaxial testing.

Overall, the comprehensive analysis of the results highlights the effectiveness of GGBFS treatment in improving the mechanical performance of sandy soil, thereby presenting promising applications for road construction projects and other geotechnical applications.

Data availability

All data generated or analysed during this study are included in this published article.

Received: 27 August 2024; Accepted: 22 January 2025

Published online: 28 January 2025

References

- Amhadi, T. S. & Assaf, G. J. Strength and permeability potentials of cement-modified desert sand for roads construction purpose. *Innov. Infrast. Solut.* **5**(3), 79 (2020).
- Rivera, J. F., Orobio, A., Cristelo, N. & de Gutierrez, R. M. Fly ash-based geopolymers as A4 type soil stabiliser. *Transp. Geotech.* **25**, 100409 (2020).
- Kazemian, S., Huat, B. B., Arun, P. & Barghchi, M. A review of stabilization of soft soils by injection of chemical grouting. *Aust. J. Basic Appl. Sci.* **4**(12), 5862–5868 (2010).
- Scrivener, K. L., Environment, U., John, V. M. & Gartner, E. M. Eco-efficient cements: potential economically viable solutions for a low-CO₂ cement-based materials industry. *Cem. Concr. Res.* **114**, 2–26 (2018).
- Miraki, H. et al. Clayey soil stabilization using alkali-activated volcanic ash and slag. *J. Rock Mech. Geotech. Eng.* **14**(2), 576–591 (2022).
- Lemounga, P. N. et al. Review on the use of volcanic ashes for engineering applications. *Resour. Conserv. Recycl.* **137**, 177–190 (2018).
- Higgins, D. *Briefing: GGBS and sustainability* (Thomas Telford Ltd, 2007).
- Gao, T., Shen, L., Shen, M., Liu, L. & Chen, F. Analysis of material flow and consumption in cement production process. *J. Clean. Prod.* **112**, 553–565 (2016).
- Davidovits, J. Years of successes and failures in geopolymer applications. Market trends and potential breakthroughs, in *Geopolymer 2002 Conference* (Geopolymer Institute Saint-Quentin, France, 2002).
- Tong, K. T., Vinai, R. & Soutsos, M. N. Use of Vietnamese rice husk ash for the production of sodium silicate as the activator for alkali-activated binders. *J. Clean. Prod.* **201**, 272–286 (2018).
- Corrêa-Silva, M. et al. Geomechanical behaviour of a soft soil stabilised with alkali-activated blast-furnace slags. *J. Clean. Prod.* **267**, 122017 (2020).
- Duxson, P. et al. Geopolymer technology: The current state of the art. *J. Mater. Sci.* **42**, 2917–2933 (2007).
- Özbay, E., Erdemir, M. & Durmuş, H. İ. Utilization and efficiency of ground granulated blast furnace slag on concrete properties—A review. *Constr. Build. Mater.* **105**, 423–434 (2016).
- Komaei, A., Soroush, A., Fattahi, S. M. & Ghanbari, H. Wind erosion control using alkali-activated slag cement: Experimental investigation and microstructural analysis. *J. Environ. Manag.* **344**, 118633 (2023).
- de Araújo, M. T., Ferrazzo, S. T., Chaves, H. M., da Rocha, C. G. & Consoli, N. C. Mechanical behavior, mineralogy, and microstructure of alkali-activated wastes-based binder for a clayey soil stabilization. *Constr. Build. Mater.* **362**, 129757 (2023).
- Syed, M., GuhaRay, A. & Raju, S. Subgrade strength performance behavior of alkali-activated binder and cement stabilized expansive soil: A semifield study. *J. Mater. Civ. Eng.* **35**(10), 04023329 (2023).
- Mypati, V. N. & Saride, S. Feasibility of alkali-activated low-calcium fly ash as a binder for deep soil mixing. *J. Mater. Civ. Eng.* **34**(1), 04021410 (2022).
- Pourakbar, S. et al. Stabilization of clay soil using alkali-activated sewage sludge. *J. Rock Mech. Geotech. Eng.* <https://doi.org/10.1016/j.jrmge.2024.09.029> (2024).
- Rios, S., Ramos, C., Viana, A., da Fonseca, N. & Cruz, C. R. Mechanical and durability properties of a soil stabilised with an alkali-activated cement. *Eur. J. Environ. Civ. Eng.* **23**(2), 245–267 (2019).
- Martins Lima, B., Bruschi, G. J., Festugato, L. & Consoli, N. C. Mechanical behavior of a granular soil stabilized with alkali-activated waste. *J. Mater. Civ. Eng.* **36**(1), 04023485 (2024).
- Han, X. et al. Effects of biochar-amended alkali-activated slag on the stabilization of coral sand in coastal areas. *J. Rock Mech. Geotech. Eng.* **15**(3), 760–772 (2023).
- Disfani, M. M., Mohammadinia, A., Arulrajah, A., Horpibulsuk, S. & Leong, M. Lightly stabilized loose sands with alkali-activated fly ash in deep mixing applications. *Int. J. Geomech.* **21**(3), 04021011 (2021).
- Kianynejad, M., Toufigh, M. M. & Toufigh, V. Mechanical performance of alkali-activated stabilized sandy soil reinforced with glass wool residue microfibers. *KSCE J. Civ. Eng.* **28**(2), 581–595 (2024).
- Elahi, M. M. A., Hossain, M. M., Karim, M. R., Zain, M. F. M. & Shearer, C. A review on alkali-activated binders: materials composition and fresh properties of concrete. *Constr. Build. Mater.* **260**, 119788 (2020).
- Li, L., Xie, J., Zhang, B., Feng, Y. & Yang, J. A state-of-the-art review on the setting behaviours of ground granulated blast furnace slag and metakaolin-based alkali-activated materials. *Constr. Build. Mater.* **368**, 130389 (2023).
- Ladd, R. Preparing test specimens using undercompaction. *Geotech. Test. J.* **1**(1), 16–23 (1978).
- D1633-17A. *Standard Test Methods for Compressive Strength of Molded Soil-Cement Cylinders* (American Society for Testing and Materials, 2017).
- ASTM.D4767-11. *Standard Test Methods for Consolidated Undrained Triaxial Compression Test for Cohesive Soils* (American Society for Testing and Materials, 2020).
- Consoli, N. C., Prietto, P. D. & Ulbrich, L. A. Influence of fiber and cement addition on behavior of sandy soil. *J. Geotech. Geoenviron. Eng.* **124**(12), 1211–1214 (1998).
- Baxter, C. D., Ravi Sharma, M., Moran, K., Vaziri, H. & Narayanasamy, R. Use of $A = 0$ as a failure criterion for weakly cemented soils. *J. Geotech. Geoenviron. Eng.* **137**(2), 161–170 (2011).
- Kamath, M., Prashant, S. & Kumar, M. Micro-characterisation of alkali activated paste with fly ash-GGBS-metakaolin binder system with ambient setting characteristics. *Constr. Build. Mater.* **277**, 122323 (2021).

32. Li, N., Shi, C., Wang, Q., Zhang, Z. & Ou, Z. Composition design and performance of alkali-activated cements. *Mater. Struct.* **50**, 1–11 (2017).
33. Provis, J. L., Palomo, A. & Shi, C. Advances in understanding alkali-activated materials. *Cem. Concr. Res.* **78**, 110–125 (2015).
34. Li, F., Liu, L., Yang, Z. & Li, S. Physical and mechanical properties and micro characteristics of fly ash-based geopolymer paste incorporated with waste granulated blast furnace slag (GBFS) and functionalized multi-walled carbon nanotubes (MWCNTs). *J. Hazard. Mater.* **401**, 123339 (2021).
35. Komaei, A., Soroush, A., Fattahi, S. M. & Ghanbari, H. Influence of environmental stresses on the durability of slag-based alkali-activated cement crusts for wind erosion control. *Sci. Tot. Environ.* **902**, 166576 (2023).
36. Palomo, A., Maltseva, O., Garcia-Lodeiro, I. & Fernández-Jiménez, A. Portland versus alkaline cement: continuity or clean break: “a key decision for global sustainability”. *Front. Chem.* **9**, 705475 (2021).
37. Ghadir, P. & Razeghi, H. R. Effects of sodium chloride on the mechanical strength of alkali activated volcanic ash and slag pastes under room and elevated temperatures. *Constr. Build. Mater.* **344**, 128113 (2022).
38. Razeghi, H. R., Ghadir, P. & Javadi, A. A. Mechanical strength of saline sandy soils stabilized with alkali-activated cements. *Sustainability* **14**(20), 13669 (2022).
39. Zhang, P. et al. Self-cementation solidification of heavy metals in lead-zinc smelting slag through alkali-activated materials. *Constr. Build. Mater.* **249**, 118756 (2020).
40. Rios, S., Cristelo, N., da Viana, F. A. & Ferreira, C. Structural performance of alkali-activated soil ash versus soil cement. *J. Mater. Civ. Eng.* **28**(2), 04015125 (2016).
41. Samantasinghar, S. & Singh, S. P. Strength and durability of granular soil stabilized with FA-GGBS geopolymer. *J. Mater. Civ. Eng.* **33**(6), 06021003 (2021).
42. Ibrahim, M., Johari, M. A. M., Rahman, M. K. & Maslehuddin, M. Effect of alkaline activators and binder content on the properties of natural pozzolan-based alkali activated concrete. *Constr. Build. Mater.* **147**, 648–660 (2017).
43. Ghadakpour, M., Choobasti, A. J. & Kutanaei, S. S. Experimental study of impact of cement treatment on the shear behavior of loess and clay. *Arab. J. Geosci.* **13**, 1–11 (2020).
44. Yang, J., Cai, X., Guo, X.-W. & Zhao, J.-L. Effect of cement content on the deformation properties of cemented sand and gravel material. *Appl. Sci.* **9**(11), 2369 (2019).
45. Du, J., Zheng, G., Liu, B., Jiang, N.-J. & Hu, J. Triaxial behavior of cement-stabilized organic matter-disseminated sand. *Acta Geotech.* **16**, 211–220 (2021).
46. Amini, Y. & Hamidi, A. Triaxial shear behavior of a cement-treated sand–gravel mixture. *J. Rock Mech. Geotech. Eng.* **6**(5), 455–465 (2014).
47. Haeri, S. M., Hosseini, S. M., Toll, D. G. & Yasrebi, S. S. The behaviour of an artificially cemented sandy gravel. *Geotech. Geol. Eng.* **23**, 537–560 (2005).

Author contributions

Mohammad Banaian: Conceptualization, Methodology, Investigation, Formal analysis, Validation, Visualization, Writing—Original Draft. Seyed Mohammad Fattahi: Supervision, Conceptualization, Project administration, Methodology, Writing—Review and Editing. Abbas Soroush: Supervision, Conceptualization; Writing—Review and Editing. Alireza Komaei: Writing—Review and Editing, Methodology, Investigation.

Declarations

Competing interests

The authors declare no competing interests.

Additional information

Correspondence and requests for materials should be addressed to S.M.F.

Reprints and permissions information is available at www.nature.com/reprints.

Publisher's note Springer Nature remains neutral with regard to jurisdictional claims in published maps and institutional affiliations.

Open Access This article is licensed under a Creative Commons Attribution-NonCommercial-NoDerivatives 4.0 International License, which permits any non-commercial use, sharing, distribution and reproduction in any medium or format, as long as you give appropriate credit to the original author(s) and the source, provide a link to the Creative Commons licence, and indicate if you modified the licensed material. You do not have permission under this licence to share adapted material derived from this article or parts of it. The images or other third party material in this article are included in the article's Creative Commons licence, unless indicated otherwise in a credit line to the material. If material is not included in the article's Creative Commons licence and your intended use is not permitted by statutory regulation or exceeds the permitted use, you will need to obtain permission directly from the copyright holder. To view a copy of this licence, visit <http://creativecommons.org/licenses/by-nc-nd/4.0/>.

© The Author(s) 2025